

Platinum (II) Nanofibers as Assembly-driven Inhibitors of Metabolic Adaptation in Cancer Cells

Zhixuan Zhou¹, Konrad Maxeiner¹, Pierpaolo Moscariello¹, Siyuan Xiang¹, Yingke Wu¹, Colette J. Whitfield¹, Lujuan Xu¹, Anke Kaltbeitzel¹, Shen Han¹, David Mücke², Haoyuan Qi^{2,3}, Manfred Wagner¹, Ute Kaiser², Katharina Landfester¹, Ingo Lieberwirth¹, David Y.W. Ng^{1,*}, Tanja Weil^{1,*}

¹ Max Planck Institute for Polymer Research, 55128 Mainz, Germany.

² Central Facility of Materials Science Electron Microscopy, Universität Ulm, 89081 Ulm, Germany.

³ Faculty of Chemistry and Food Chemistry & Center for Advancing Electronics Dresden (cfaed), Technische Universität Dresden, 01062 Dresden, Germany.

Abstract

Nanostructure-based functions are omnipresent in biology and essential for the diversity of life. Despite their importance, it is difficult to establish mechanisms that define their bioactivity and rationalize them through synthetic designs. As such, strategies that connect bioactive functions through structure formation are scarce. Herein, we design a near-infrared emitting platinum (II)-tripeptide that undergoes a rearrangement using endogenous H₂O₂ to rapidly assemble into fibrillar superstructures. The resultant assembly inhibits the metabolism of aggressive metastatic MDA-MB-231 cells and A549 cells at the systemic level by blocking aerobic glycolysis and oxidative phosphorylation, thereby shutting down ATP production. Hence, ATP-dependent actin formation and glucose metabolite-dependent histone deacetylase activity are downregulated, leading to apoptosis. By demonstrating that assembly-driven functions can inhibit broad biological pathways, supramolecular nanostructures could offer the next generation biomedical solutions beyond conventional applications.

Introduction

In cells, protein nanostructures are abundant, serving as cellular scaffolds, multi-domain catalysts, and transport highways¹. Among them, ordered protein assemblies consisting of β -sheet structures, so-called β -amyloids, play both functional and pathological roles. They serve as biotemplates, within melanocytes, for melanin biosynthesis^{2,3} or as nucleating centers towards the amyloidosis in Type 2 diabetes^{4,5}. Mechanistically, the monomers of these ordered nanostructures do not possess intrinsic functions of their own, but rely on the propagation of long-range hierarchical structures to feature their rich biological activities.

Several strategies have since attempted to re-engineer these nanostructures using simplified peptide-based monomers to elicit biomedical functions⁶⁻¹³. Pharmacologically, self-assembling nanostructures in cells combine features of small molecules such as deep cell/tissue penetration together with properties from larger superstructures like enzymatic stability and retardation of cellular efflux^{10,14,15}. However, in contrast to molecular drugs and prominent biologics, such as antibodies or mRNA, which target a specific enzyme, receptor or gene expression, very little is known on the biochemical profile of intracellularly self-assembled nanostructures. We rationalized that nanostructures could plausibly exhibit broad bioactivity on a systemic level that impacts multiple biological pathways simultaneously.

In this regard, metabolism is a critical set of processes that define cellular life, and it has witnessed increasing focus due to the rising significance of aerobic glycolysis (AGlyc) in cancer cells¹⁶⁻¹⁸. Also termed as the Warburg effect, AGlyc upregulates the processing of glucose to produce ATP in the presence of oxygen while paradoxically competing against a more efficient oxidative phosphorylation pathway (OxPhos)¹⁹. The preference for AGlyc aims to conserve anabolic carbon resources for biosynthesis required for cancer cell proliferation, whereas OxPhos breaks these resources down into CO₂ that exits cellular metabolism¹⁰. Inhibitors of AGlyc or OxPhos have recently shown great promise in addressing aggressive triple-negative MDA-MB-231 breast cancer and A549 lung cancer, which have a poor prognosis as effective therapies are currently lacking^{20,21}. Particularly in the metastatic state when cells can dynamically switch between AGlyc/OxPhos metabolism with increased drug efflux, treatment regimens with chemotherapeutics, such as cisplatin, are largely ineffective, resulting in resistances towards chemotherapies over time²².

We propose that cancer cell adaptation can be broadly targeted by assembly-driven metabolic inhibition, by blocking AGlyc/OxPhos pathways and thus ATP-dependent downstream processes. The assembly-driven metabolic inhibitor (ADMI) reported herein comprises a platinum (II) terpyridine (Pt-tpy), which serves as a near-infrared (NIR) motif promoting π - π interactions and intermolecular metal-metal alignment into ordered β -amyloid-like structures^{23,24}. Tethered to the Pt-tpy is an *iso*-tripeptide, where its isomerization between the “kinked” monomeric and linear self-assembling forms is controlled by elevated levels of reactive oxygen species (ROS) (Fig. 1a)¹¹. The structural transition into the ADMI is assessed on triple-negative MDA-MB-231 cells, derived from a highly metastatic cancer, and A549 cells. The impact of the ADMI on AGlyc/OxPhos leading to histone deacetylase (HDAC) activity, actin restructuring, and apoptosis is investigated. We demonstrate that assembly-driven functions can be leveraged as an alternative treatment modality where supramolecular structures modulate bioactivity in a complex living environment.

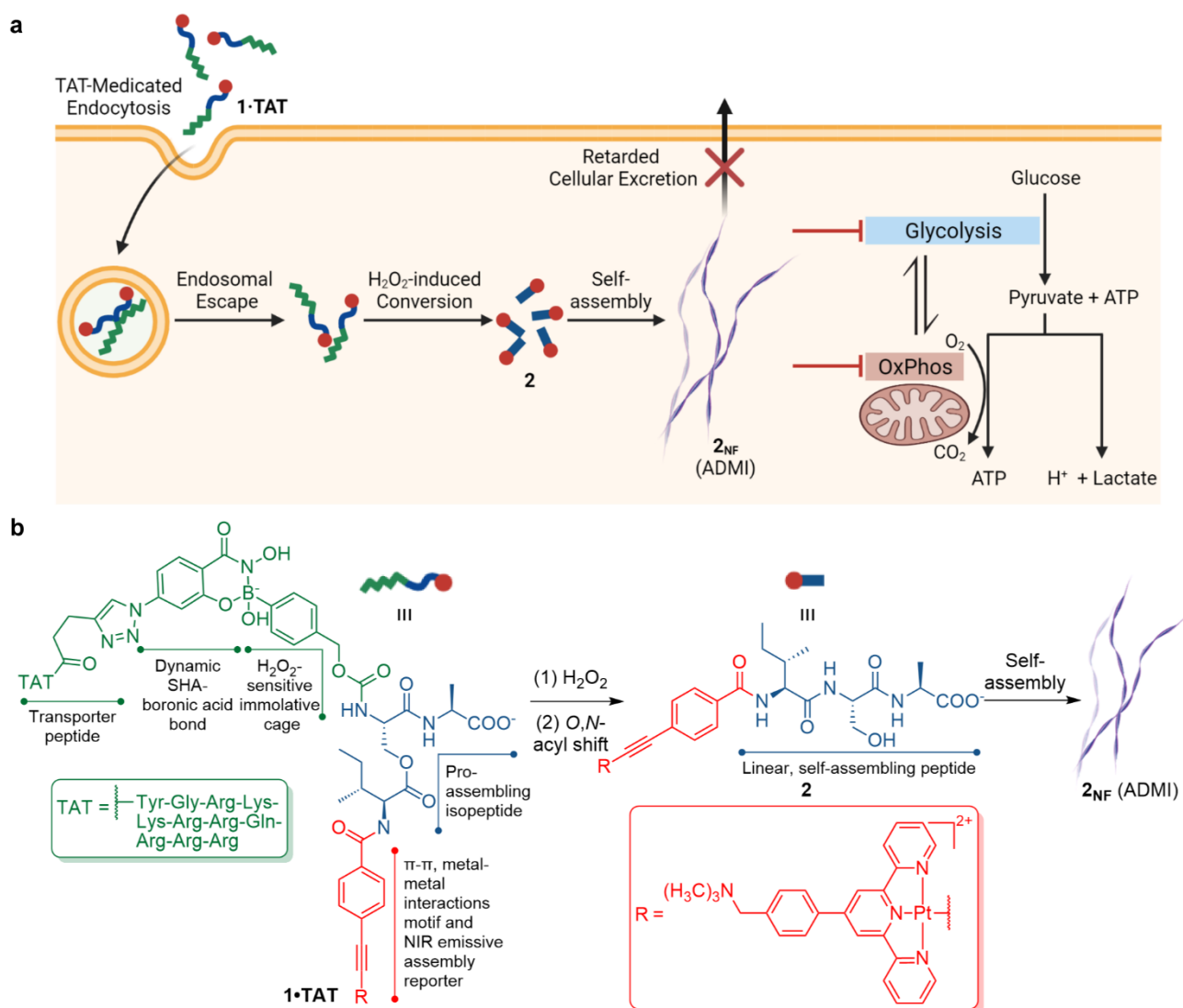


Fig. 1| Intracellular assembly of platinum (II)-containing nanofibers can disrupt aerobic cancer cell metabolism and cause cancer cell apoptosis. a, Schematic illustration of the intracellular H₂O₂-induced formation of linear platinum (II) complexes that self-assemble into nanofibers, which inhibit cell metabolism. **b**, Chemical design for the trans-activator of transcription (TAT) peptide appended isopeptide-platinum (II) complex **1·TAT** and its reaction scheme for intracellular H₂O₂-induced conversion to linear complex **2**, which then undergoes self-assembly in the cytosol to form nanofibers **2_{NF}**.

Design and H₂O₂ cascade transformation of ADMI precursors

The isopeptide-platinum (II) complex **1·TAT** is composed of three functional modules (Fig. 1b): 1) a pro-assembling isopeptide (ISA) caged by an immolative boronic acid group¹¹, 2) a transporter peptide (trans-activator of transcription, TAT)²⁵ connected to the boronic acid group via a dynamic covalent salicylhydroxamate (SHA)-boronic acid bond²⁶, and 3) a Pt-tyr complex coordinated to the alkynyl group on the N-terminus of the ISA peptide. The expected mechanism of how the complex interacts with cells would begin with the TAT-mediated endocytosis and intracellular endosomal escape of the complex¹¹. Only at near-neutral (pH 7.4) cytosolic conditions, endogenous H₂O₂ possess sufficient oxidative strength to immolate the boronic acid cage¹¹. The exposed –NH₂ of the serine residue

undergoes an *O,N*-acyl shift, causing the peptide to rapidly isomerize into the monomeric assembly precursor **2** (Supplementary Fig. 27), which assembles into the ADMI nanofibers **2**_{NF}.

The kinetics of the H₂O₂-triggered formation of **2** in solution was investigated by high performance liquid chromatography-mass spectrometry (LC-MS) (Fig. 2a–d, Supplementary Fig. 28). In aqueous solution, incubation with H₂O₂ for 20 min resulted in the complete disappearance of **1** and the emergence of two new peaks with retention times (*t*_R) of 5.69 min and 6.06 min, respectively (Fig. 2b) both showing *m/z* values in agreement with the chemical formula of **2** (*m/z* = 496.4 for [**2** + H]⁺ and 991.3 for [**2**]²⁺) (Fig. 2c, Supplementary Fig. 29). In comparison with **2** obtained via synthesis (*t*_R = 6.06 min), the former was assigned to be the intermediate formed (*iso-2*) upon the immolation of the phenylboronic acid prior to isomerization. Further incubation with H₂O₂ led to an increase of **2**, with a 95% conversion at 4 h (Fig. 2d). In contrast, less than 5% conversion was observed after 24 h incubation of **1** without H₂O₂ (Supplementary Fig. 30).

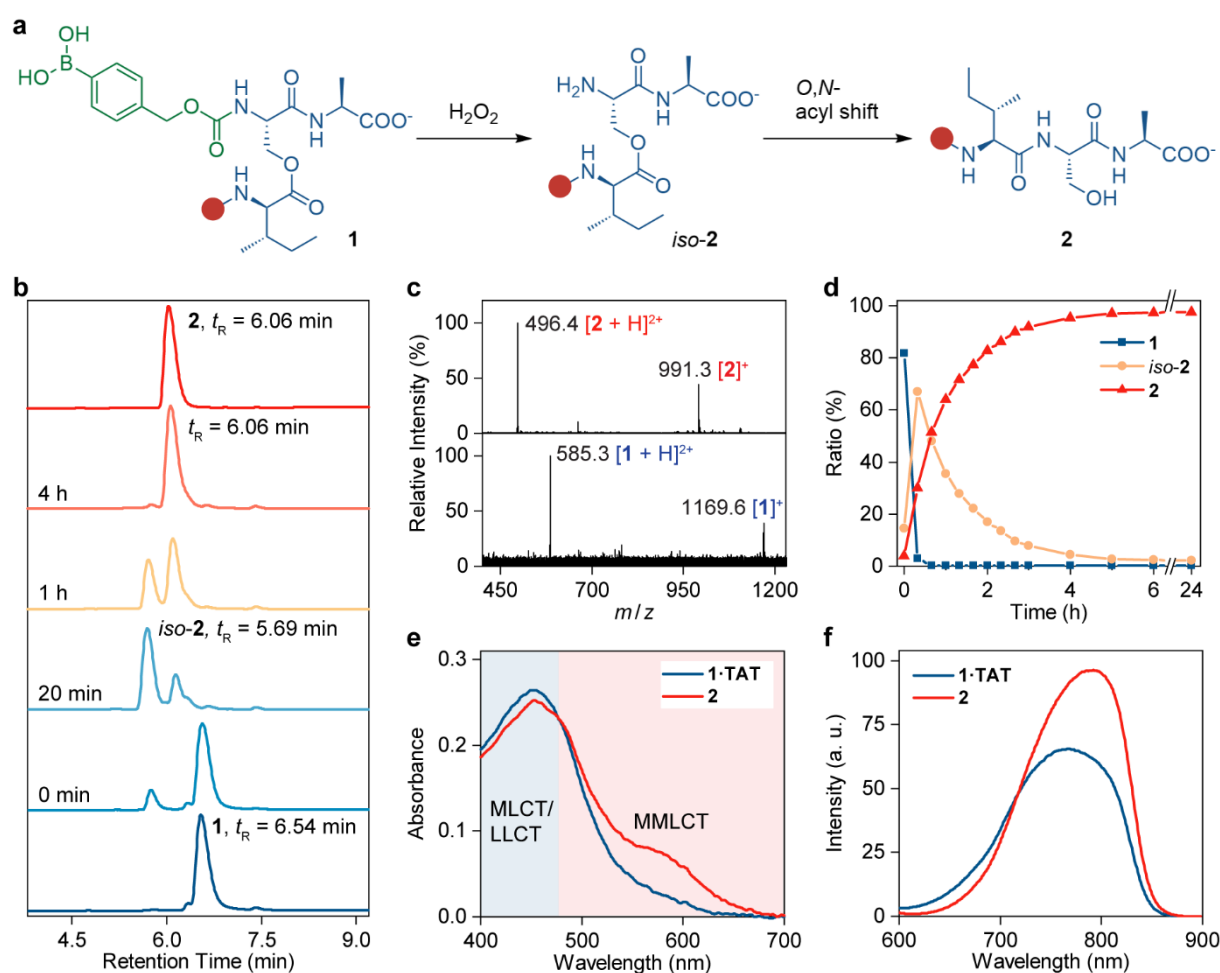


Fig. 2| H₂O₂-induced formation of **2 in PB.** **a**, Reaction scheme for the conversion of **1** to **2** in H₂O₂ in near-neutral pH. H₂O₂ removes the phenylboronic acid cage, leading to the formation of intermediate *iso-2* with free -NH₂. Subsequent *O,N*-acyl rearrangement of the isopeptide bond in *iso-2* generates **2**. **b**, LC-MS kinetic analysis over the H₂O₂ (0.5 mM)-induced linearization of **1** (50 μM) in a mixture of NH₄HCO₃ buffer (pH 7.4, 20 mM) and CH₃OH (9/1, vol%). **c**, Convolved MS spectra in the LC-MS analysis for a reaction time of 0 min and *t*_R = 6.06–6.21 s (identified as complex **1**) and a reaction time of 4 h and *t*_R = 6.54–6.69 s (identified as complex **2**). **d**, Molar ratio of **1**, *iso-2* and **2** after addition of H₂O₂ based on the peak integration at 254 nm. **e**, UV-Vis

absorption spectra of **1-TAT** and **2** (50 μ M) in PB (pH 7.4, 50 mM). **f**, Luminescence emission spectra of **1-TAT** and **2** (50 μ M) in PB (pH 7.4, 50 mM). Excitation wavelength = 488 nm.

The square-planar platinum (II) center in the complexes endows the ADMI with optical properties associated with the nature of self-assembly. Complexes **1-TAT** and **2** displayed absorption bands centered at 460 nm in PB (Fig. 2e), which can be assigned to a combination of $d\pi(\text{Pt}) \rightarrow \pi^*(\text{tpy})$ metal-to-ligand charge-transfer (MLCT) and alkynyl-to-tpy ligand-to-ligand charge-transfer (LLCT) transitions. A lower energy absorption shoulder at ca. 570 nm is observed for both complexes, which can be attributed to a metal-metal-to-ligand charge-transfer (MMLCT) transition^{23,27}. Complex **2** exhibited weaker MLCT/LLCT transition but markedly stronger MMLCT absorption than **1-TAT**. This indicates a higher extent of intermolecular d_z^2 interactions between platinum (II) centers in neighboring molecules of **2**, suggesting a proclivity for self-assembly in PB forming **2_{NF}**^{23,27}. Both solutions showed NIR emission originating from the MMLCT excited states upon excitation at 488 nm (Fig. 2f). Complex **1-TAT** exhibited emission centered at 770 nm, whereas complex **2** displayed red-shifted emission ($\lambda_{\text{max}} = 792$ nm) with a 1.5-fold higher intensity, which can be ascribed to the enhanced MMLCT transition as a result of self-assembly. The difference in the photophysical profile between the solutions of the complexes facilitate the tracking of their H_2O_2 -induced conversion and subsequent assembly of **2** into **2_{NF}** in PB. Treatment of **1-TAT** with H_2O_2 (0.5 mM) led to a red-shift in the λ_{max} with a concomitant increase in emission intensity (Supplementary Fig. 31). The conversion is completed in 280 min with the final emission profile resembling that of **2_{NF}**, in agreement with the LC-MS study.

ADMI nanofibers **2_{NF}** show high molecular order.

The self-assembly of the complexes were visualized using transmission electron microscopy (TEM). Nanofibers were observed for **2_{NF}** at concentrations ranging from 5 to 100 μ M (Fig. 3a, Supplementary Fig. 32), whereas **1** and **1-TAT** showed no defined nanostructures (Supplementary Fig. 33). Upon oxidation of **1-TAT** by H_2O_2 , the transformation into **2** and subsequent self-assembly produced similar fibrous morphology to the control (Supplementary Fig. 34). Selected-area electron diffraction on **2_{NF}** showed diffraction arcs with 3.3 Å lattice spacing, in agreement with the intermolecular distance of π - π interactions within the nanofibers²⁸. The diffraction arcs are perpendicular to the long axis of the fibers (Fig. 3b, Supplementary Fig. 35). Nanofiber formation is further supported by cryogenic high-resolution TEM studies on **2_{NF}** in PB, where the growth axis suggested an end-to-end molecular arrangement of the complexes (Fig. 3c, Supplementary Fig. 36). Each fiber was observed to be bundled with a mean interfiber distance of 2.9 nm.

Circular dichroism (CD) spectroscopy analysis on **2_{NF}** revealed a maximum at 190 nm corresponding to the $\pi \rightarrow \pi^*$ of the carbonyl group, depicting H-bond interactions centered on the peptidic backbone. This is coupled with the red-shifted $n \rightarrow \pi^*$ transition visible at the 229 nm minimum²⁹. Exciton coupling parallel to the peptide backbone also exists for **2_{NF}** at 210 nm²⁹ (Fig. 3d). Additionally, a strong positive signal beyond 250 nm corresponding to the $\pi \rightarrow \pi^*$ transition of the Pt-tpy group²³ is also observed for **2_{NF}**, demonstrating the importance of the Pt-tpy group in the self-assembly. In contrast, **1** only exhibited a minimum at 208 nm (Supplementary Fig. 37). The self-assembly behavior of **2_{NF}** at the

molecular level was further examined using NMR. At 298 K, **2_{NF}** showed broad signals in the ¹H NMR spectrum. Increasing the temperature led to sharpening of the signals accompanied by significant downfield shifts (Supplementary Fig. 39), which indicates self-assembly at 298 K. Nuclear Overhauser effect spectroscopy (NOESY) of **2_{NF}** revealed NOE cross peaks between the protons on the tpy group and the phenyl ring of the alkynyl ligand (*H^d/H^h* and *H^e/H^h*), and between the non-neighboring protons on the tpy moiety (*H^b/H^e*, *H^b/H^d*, and *H^b/H^e*) (Fig. 3e, Supplementary Fig. 45), implying that the Pt-tpy group adopt a twisted head-to-tail stacking upon self-assembly (Fig. 3f), which is characteristic for Pt-tpy complexes²⁷. The microscopy and spectroscopy experiments suggest that **2_{NF}** possesses a high degree of molecular order, which is highly favorable for studies in a biological context because it enhances the proteolytic stability of the nanofibers and promotes NIR emission originated from the Pt-tpy group (Fig. 3g).

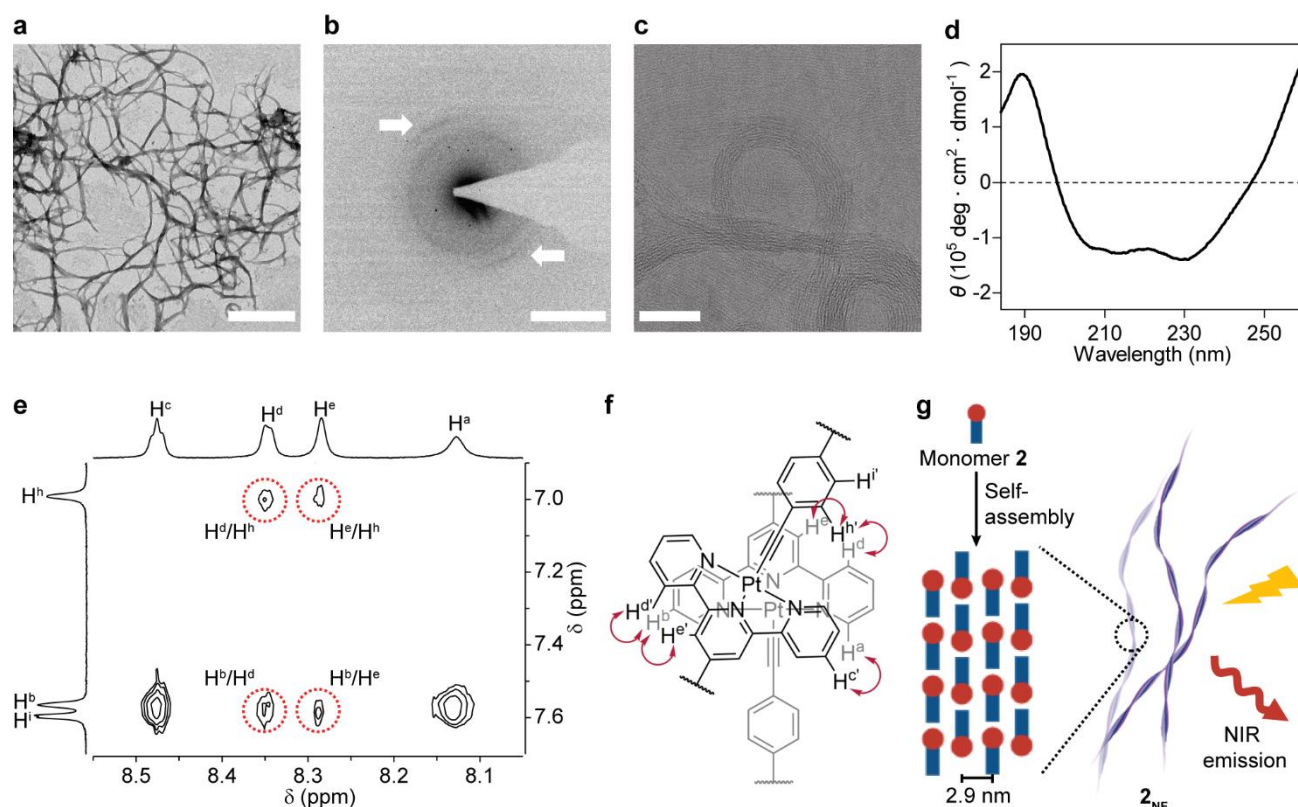


Fig. 3| Nanofiber **2_{NF} with a high degree of molecular order formed by self-assembly of **2**.** **a**, TEM image of the nanofibers **2_{NF}** (25 μM) in PB (pH 7.4, 10 mM). Scale bar, 200 nm. **b**, Selected-area electron diffraction pattern of the nanofiber **2_{NF}** (100 μM) in H₂O. The white arrows indicate diffraction arcs at 3.0 nm⁻¹, i.e., 3.3 Å. Scale bar, 3 nm⁻¹. **c**, Cryogenic high-resolution TEM image of the nanofiber **2_{NF}** (25 μM) in PB (pH 7.4, 10 mM). Scale bar, 50 nm. **d**, Circular dichroism (CD) spectra of **2_{NF}** in a mixture of PB (pH 7.4, 10 mM) and CH₃CN (98/2, vol%). **e**, Partial ¹H, ¹H NOESY NMR spectrum (850 MHz, 343K) of **2** (1 mg/mL) in PB (pH 7.4, 50 mM). Intermolecular NOE cross-peaks are circled in the NMR spectrum. **f**, Proposed molecular stacking mode of the Pt-tpy group in **2_{NF}** based on the NOESY NMR study. Red arrows indicate intermolecular NOE interactions between protons. **g**, Proposed arrangement of monomer **2** in **2_{NF}** based on microscopy and NMR studies. The nanofibers showed a mean interfiber distance of 2.9 nm. Nanofiber formation also promotes NIR emission originated from the Pt-tpy groups in **2_{NF}**.

Intracellular formation of ADMI **2_{NF}** induces actin restructuring

The growth of the nanofibers **2_{NF}** was visualized in A549 lung alveolar adenocarcinoma cells and MDA-MB-231 metastatic breast cancer cells using confocal laser scanning microscopy (Fig. 4a, Supplementary Figs 46 and 47). Within 4 h, TAT-dependent internalization of **1-TAT** (25 μ M) was observed (Fig. 4a). Assisted by the NIR emission of the platinum (II) center, correlative light-electron microscopy (CLEM) observed that newly formed luminescent nanofibers within the cytoplasm occur after escape from the endosomal vesicles (Fig. 4b, Supplementary Figs 48 and 49). In line with the pH-dependence of endogenous H₂O₂ activity on the boronic acid, the TEM micrographs revealed that the entry into the near-neutral (pH 7.4) cytosol from the acidic (pH 6.0) endosomes initiates the nanofiber formation. At the onset of nanofiber growth, the first metabolic consequence of newly formed ADMI **2_{NF}** can be detected through early changes in the cytoskeleton, whose formation is tightly coupled to glycolytic pathways^{30,31}. An investigation using cytoskeleton stain Phalloidin-iFluorTM 405 demonstrated a restructuring of actin filaments towards the cellular membrane (Fig. 4c, Supplementary Fig 52). Using both 10 μ M and 25 μ M, the appearance of fluorescent loci along the cell membrane was only observed at 25 μ M (Fig. 4c, lower panel), suggesting that a critical concentration threshold of **2_{NF}** has to be reached for actin restructuring.

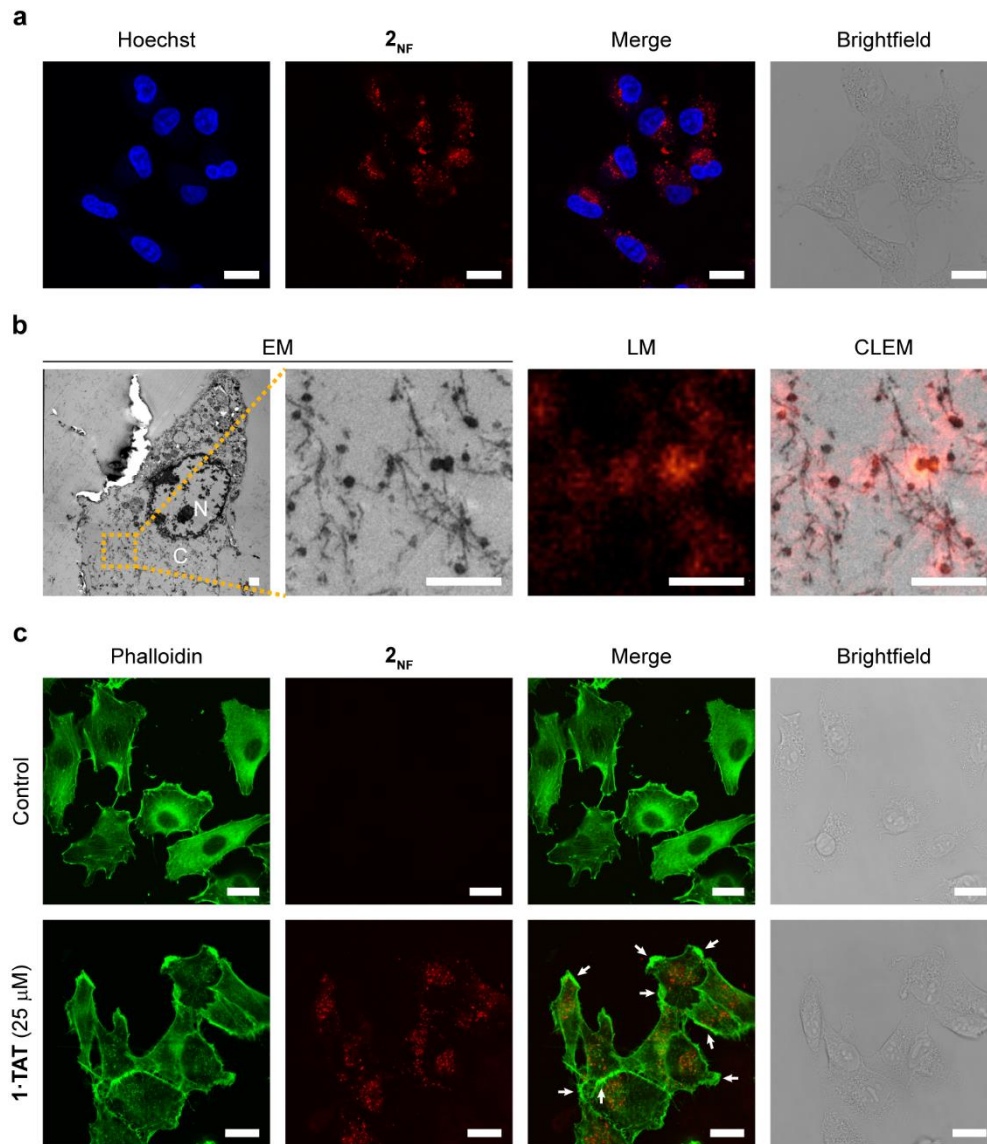


Fig. 4| Internalization of 1-TAT and assembly into ADM1 nanofibers 2_{NF} in the cytoplasm that restructure actin filaments. a, Confocal laser scanning micrographs of A549 cells treated for 4 h with **1-TAT** (25 μ M) and Hoechst 33342 dye. Scale bars, 20 μ m. **b**, CLEM of A549 cells treated for 6 h with **1-TAT** (50 μ M). N, nucleus. C, Cytosol. Scale bars, 1 μ m. **c**, Confocal laser scanning micrographs of A549 cells treated for 4 h with **1-TAT** (25 μ M) and Phalloidin-iFluor™ 405. White arrows indicate the fluorescent loci along the cell membrane. Scale bars, 20 μ m.

ADMI nanofibers 2_{NF} inhibit AGlyc and OxPhos metabolic pathways

We investigate the impact of the ADMI 2_{NF} on the main mechanisms of cellular metabolism, AGlyc and OxPhos pathways, which are core upstream processes involving at least 10% of the human proteome³². In cancer cells, metabolism is particularly altered to sustain perpetual growth, metastasis, and the unconventional use of glucose in the presence of oxygen¹⁶⁻¹⁹. Both the consumption of oxygen to fuel mainly OxPhos, and the extracellular acidification as a function of AGlyc were analyzed in A549 and MDA-MB-231 cells using a Seahorse® Extracellular Flux Analyzer (Fig. 5). Treatment of both cell lines with 1-TAT to form the ADMI 2_{NF} demonstrated a reduction in the oxygen consumption rate (OCR) within 4 h (Fig. 5c), with 25 μ M or 10 μ M inducing respectively a 41-fold and a 7-fold decrease (Fig. 5d). The OCR, expressed as pmol/min, is a first measure of OxPhos (Fig. 5a, b) activity, which take place primarily in the mitochondria.

Key parameters of mitochondrial respiration were investigated to unravel more in detail the impact of the ADMI on OxPhos by sequential use of modulators of the electron transport chain (ETC): rotenone (Complex I), antimycin A (Complex III) and oligomycin (ATP synthase) and FCCP (Carbonyl cyanide 4-(trifluoromethoxy)phenylhydrazone) disrupting the mitochondrial membrane potential^{33,34}. Treated cells exhibit less than 10% of the FCCP-induced maximal respiration compared to untreated cells, highlighting the inability of cells to address a challenging energy demand when stimulated to operate at maximum capacity. (Fig. 5e). Thus, in addition to the impact on OxPhos depicted by the acute response, the ADMI induces a massive and more stable effect on mitochondrial respiration that prevents cells from adapting to stress. This phenomenon is further confirmed by a reduction of most of the OxPhos-related parameters, such as ATP production, spare respiratory capacity, and proton leak, which is a potential indicator of mitochondrial damage (Supplementary Figs 55, 56). Based on the ADMI burden on mitochondrial respiration, we subsequently evaluated parameters related to AGlyc where cancer cells are known for being able to rewire their cell metabolism between OxPhos and AGlyc, upregulating accordingly one of the two metabolic pathways to meet their energetic needs.

Therefore, the AGlyc of A549 and MDA-MB-231 cells was measured using their extracellular acidification rate (ECAR_{glyc}), expressed as mpH/min (Fig. 5f–g). Extracellular acidification occurs when glucose is converted to pyruvate and lactate, accompanied by the extrusion of protons into extracellular space³⁵ (Fig. 5f). The cells first underwent glucose starvation to account for the basal non-glycolytic acidification, followed by the addition of saturating amounts of glucose to trigger glycolysis. The formation of the nanofibers at 25 μ M shuts down glycolysis of A549 and MDA-MB-231 to $6 \pm 1\%$ and $13 \pm 3\%$, respectively (Fig. 5i). The capability of cancer cells rewiring their metabolism³⁶ was demonstrated by adding oligomycin, the ATP synthase inhibitor³³, to shut down OxPhos and thereby inducing the switch to glycolysis. In the untreated control cells, the incubation with oligomycin raised the glycolytic activity by $+11.5 \pm 4.0$ mpH/min (A549) as well as $+8.2 \pm 3.5$ mpH/min (MDA-MB-231) (Fig. 5j). This adaptation is termed as the glycolytic reserve, which is activated upon mitochondrial stress/dysfunction.

In comparison to cells where the ADMI is formed, inhibition of OxPhos by oligomycin increased the glycolytic acidification by only 0.5 mpH/min for A549 cells and 0.2 mpH/min for MDA-MB-231 cells (Fig. 5h). Hence, even under severe stress conditions, aerobic glycolysis remained low, suggesting that the capabilities of the cells to compensate this inhibited pathway was limited. To further ascertain that the extracellular acidification is the consequence of glucose metabolism, 2-deoxy-glucose, a

competitive inhibitor towards glucose hexokinase³³ was added. By inhibiting the first enzyme of glycolysis and thus the suppression of ECAR, we demonstrated that the observed extracellular acidification is an accurate measure of their glycolytic activities. In summary, ADMI have shown the ability to impair cancer cell fitness by interfering with both OxPhos and AGlyc and preventing metabolic adaptation, one of the most characteristic features that cancer cells use to react and address stress stimuli³⁷. In A549 cells, apoptotic resistance have been linked to the attenuation of OxPhos while increasing the rate of glycolysis, and that targeting OxPhos have led to reduced drug resistance¹⁷ and cancer proliferation³⁸. Similarly, in MDA-MB-231, among the most aggressive cancer subtypes with the worst prognosis, the metabolic plasticity showed an even higher relevance in clinical outcomes where the targeting both OxPhos and AGlyc is the current state-of-the-art to control its progression^{21,39,40}.

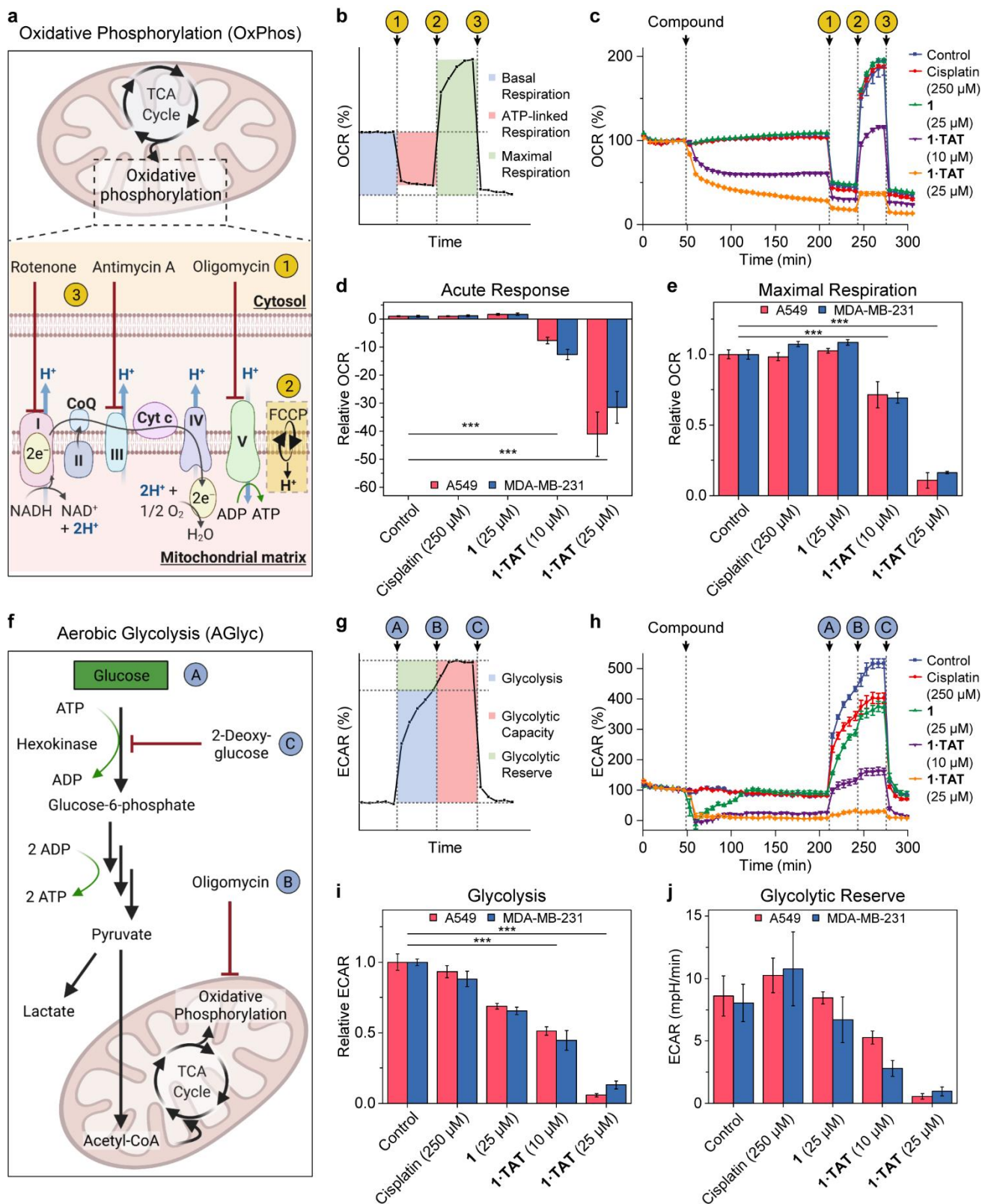


Fig. 5| ADMI 2_{NF} inhibits both AGlyc and OxPhos metabolism of A549 and MDA-MB-231 cells. a, Scheme of a mitochondrion with focus on the electron transport chain, site of oxidative phosphorylation. The compounds of the Mito stress test modulate the ETC when added in the indicated injection sequence. **b**, Profile of the oxygen consumption rate (OCR) during the Mito stress test. Numbers represent the compounds of the Mito stress test shown in Fig. 5a. **c**, Effect of the ADMI on the oxygen consumption rate of MDA-MB-231. The last measurement before treatment injection is set as 100%. **d**, **e**, Acute response (**d**) and maximal respiration (**e**)

of A549 and MDA-MB-231 cells. **f**, Schematic representation of glycolysis and cell respiration, which are affected by the compounds of the glycolysis stress test. Each target of the modulators of the glycolysis and oxidative phosphorylation used in the assay are indicated with respect to the injection sequence. **g**, Profile of the extracellular acidification rate (ECAR) during the glycolysis stress test. Characters represent the compounds of the glycolysis stress test shown in Fig. 5f. **h**, Effect of the ADMI on the extracellular acidification rate (ECAR) of MDA-MB-231. **i,j** Effect of the ADMI on the glycolysis (**i**) and glycolytic reserve (**j**) of A549 and MDA-MB-231 cells. For **d,e**, and **i** the data are expressed as relative values to untreated control cells. Data are presented as mean \pm s.e.m., $n > 5$ independent experiments. Statistical significance was calculated by ANOVA with a Tukey post hoc test. ***: $P < 0.001$.

ADMI nanofibers 2_{NF} induces early apoptosis

With the ADMI showing inhibitory activities in both AGlyc and OxPhos processes, the production of metabolites such as glucose-6-phosphate (G6P) are negatively affected. Hence, G6P related pathways such as the downstream production of NADPH by glucose-6-phosphate dehydrogenase will be challenged, leading to the downregulation of histone deacetylase (HDAC) activity⁴¹. Indeed, ADMI treated A549 and MDA-MB-231 cells showed concentration dependent reduction in HDAC activity at 4 h, with 25 μ M showing a 25% and 10% decrease, respectively (Supplementary Fig. 63). With the impairment of metabolic pathways and HDAC activity, apoptosis of the cells was evaluated using Annexin V-FITC and cell viability assays. At 25 μ M, the ADMI induced the presence of phosphatidylserine on the external leaflet of the cell membrane and was detected by the binding of Annexin V-FITC. This characteristic observation of early apoptosis suggests that the population of cells were undergoing the hallmark changes associated with programmed cell death (Fig. 6a, Supplementary Fig.64)⁴². The IC₅₀ value of the ADMI was found to be comparable for both A549 cells (60.6 μ M) and MDA-MB-231 cells (58.5 μ M) at 4 h, while the cisplatin control requires 24 h to show an effect on cell viability (Fig. 6b, Supplementary Fig. 65). Cisplatin was used as a comparison and reference due to its use as a broad-spectrum chemotherapeutics for solid malignancies even though cisplatin resistance remained a widespread problem⁴³. The disparity in time-dependent efficacies of cisplatin and the ADMI is apparent likewise in the metabolic studies, where a 4 h cisplatin treatment did not produce observable effects on AGlyc and OxPhos even at a 10-fold higher (250 μ M) concentration (Fig. 5). It is interesting to note that even though the formation of nanofibers demonstrates a more significant impact on oxygen-dependent ATP production on A549 cells compared to MDA-MB-231 cells, the IC₅₀ value of the ADMI on both cell lines (60.6 μ M/A549; 58.5 μ M/MDA-MB-231) are not significantly different. We hypothesize that upon the critical assembly concentration of the nanofibers, the damage threshold towards cellular metabolism has reached a point of no return. At this stage, any further damage on cells that are already undergoing apoptosis would not provide additional statistical weight on the overall cell viability.

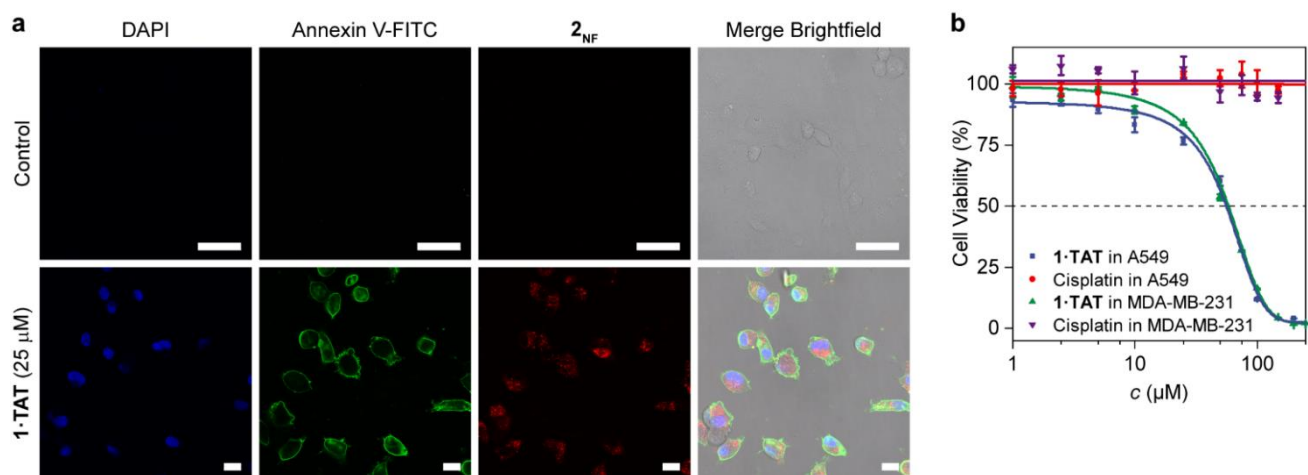


Fig. 6| Toxicity of 1-TAT towards A549 and MDA-MB-231 cells. **a**, The apoptotic nature of cell death was investigated for A549 cells using Annexin V assay. Cells were incubated 4 h with **1-TAT** (red) and treated with Annexin V (green) afterwards. Nuclei were stained using DAPI (blue). Annexin V binds to the cell membrane upon an inversion of phosphatidylserine motifs towards the extracellular space, indicating apoptosis. Scale Bars, 50 μm . **b**, Cell viability assay of A549 and MDA-MB-231 cells treated with **1-TAT** and cisplatin for 4 h, revealing viable cells after cisplatin treatment and significantly reduced cell viability after application of the ADMI. The cell viability was determined using the CellTiter-Glo Luminescence Cell Viability Assay Kit.

Conclusions

In conclusion, we have designed a pro-assembling Pt(II)-containing peptide that undergoes a step-wise transformation into a NIR emitting ADMI within A549 and MDA-MB-231 cells. The Pt-tpy complex directs the supramolecular order and directionality of the packing within the fiber axis, while providing NIR photoluminescence beyond the autofluorescence of the cells. The formation of the ADMI rapidly damages essential metabolic pathways, AGlyc and OxPhos, preventing the cells from mounting adaptive strategies that effectively resist specific small molecule inhibitors, increase aggressiveness and metastatic potential. Downstream pathways intrinsically linked to ATP production (cytoskeleton) and glucose metabolites (HDAC) are found to be impaired, thus confirming the mechanistic origin of the ADMI. Apoptosis is induced within 4 h compared with cisplatin (24 h) and found to leverage a similar impact even on different cell types. By demonstrating that complex cellular functions can be addressed purely by supramolecular order, we hope that synthetic nanostructure formation in cells can be established as an alternative therapeutic platform in the near future.

References

1. Pieters, B. J. G. E., van Eldijk, M. B., Nolte, R. J. M. & Mecinović, J. Natural supramolecular protein assemblies. *Chem. Soc. Rev.* **45**, 24-39 (2016).
2. McGlinchey, R. P. *et al.* The repeat domain of the melanosome fibril protein Pmel17 forms the amyloid core promoting melanin synthesis. *Proc. Natl. Acad. Sci. USA* **106**, 13731-13736 (2009).
3. Dean, D. N. & Lee, J. C. Defining an amyloid link Between Parkinson's disease and melanoma. *Proc. Natl. Acad. Sci. USA* **117**, 22671-22673 (2020).

4. Westermark, P., Andersson, A. & Westermark, G. T. Islet Amyloid Polypeptide, Islet Amyloid, and Diabetes Mellitus. *Physiol. Rev.* **91**, 795-826 (2011).
5. Iadanza, M. G., Jackson, M. P., Hewitt, E. W., Ranson, N. A. & Radford, S. E. A new era for understanding amyloid structures and disease. *Nat. Rev. Mol. Cell Biol.* **19**, 755-773 (2018).
6. Hendricks, M. P., Sato, K., Palmer, L. C. & Stupp, S. I. Supramolecular Assembly of Peptide Amphiphiles. *Acc. Chem. Res.* **50**, 2440-2448 (2017).
7. Goor, O. J. G. M., Hendrikse, S. I. S., Dankers, P. Y. W. & Meijer, E. W. From supramolecular polymers to multi-component biomaterials. *Chem. Soc. Rev.* **46**, 6621-6637 (2017).
8. Qi, G.-B., Gao, Y.-J., Wang, L. & Wang, H. Self-Assembled Peptide-Based Nanomaterials for Biomedical Imaging and Therapy. *Adv. Mater.* **30**, 1703444 (2018).
9. Shy, A. N., Kim, B. J. & Xu, B. Enzymatic Noncovalent Synthesis of Supramolecular Soft Matter for Biomedical Applications. *Matter* **1**, 1127-1147 (2019).
10. Yuan, Y. *et al.* Furin-mediated intracellular self-assembly of olsalazine nanoparticles for enhanced magnetic resonance imaging and tumour therapy. *Nat. Mater.* **18**, 1376-1383 (2019).
11. Pieszka, M. *et al.* Controlled Supramolecular Assembly Inside Living Cells by Sequential Multistaged Chemical Reactions. *J. Am. Chem. Soc.* **142**, 15780-15789 (2020).
12. Yang, L. *et al.* Desuccinylation-Triggered Peptide Self-Assembly: Live Cell Imaging of SIRT5 Activity and Mitochondrial Activity Modulation. *J. Am. Chem. Soc.* **142**, 18150-18159 (2020).
13. Miki, T. *et al.* Intracellular artificial supramolecules based on de novo designed Y15 peptides. *Nat. Commun.* **12** (2021).
14. Knauer, M. F., Soreghan, B., Burdick, D., Kosmoski, J. & Glabe, C. G. Intracellular accumulation and resistance to degradation of the Alzheimer amyloid A4/beta protein. *Proc. Natl. Acad. Sci. USA* **89**, 7437-7441 (1992).
15. Yuan, Y. *et al.* Intracellular Self-Assembly of Taxol Nanoparticles for Overcoming Multidrug Resistance. *Angew. Chem. Int. Ed.* **54**, 9700-9704 (2015).
16. Zhu, J. & Thompson, C. B. Metabolic regulation of cell growth and proliferation. *Nat. Rev. Mol. Cell Biol.* **20**, 436-450 (2019).
17. Vasan, K., Werner, M. & Chandel, N. S. Mitochondrial Metabolism as a Target for Cancer Therapy. *Cell Metab.* **32**, 341-352 (2020).
18. Martínez-Reyes, I. & Chandel, N. S. Cancer metabolism: looking forward. *Nat. Rev. Cancer* **21**, 669-680 (2021).
19. DeBerardinis, R. J. & Chandel, N. S. We need to talk about the Warburg effect. *Nat. Metab.* **2**, 127-129 (2020).
20. Cheng, G. *et al.* Targeting Isonidamide to mitochondria mitigates lung tumorigenesis and brain metastasis. *Nat. Commun.* **10** (2019).
21. Fiorillo, M., Scatena, C., Naccarato, A. G., Sotgia, F. & Lisanti, M. P. Bedaquiline, an FDA-approved drug, inhibits mitochondrial ATP production and metastasis in vivo, by targeting the gamma subunit (ATP5F1C) of the ATP synthase. *Cell Death Differ.* **28**, 2797-2817 (2021).
22. Icard, P. *et al.* How the Warburg effect supports aggressiveness and drug resistance of cancer cells? *Drug Resist. Updat.* **38**, 1-11 (2018).
23. Yam, V. W.-W., Chan, A. K.-W. & Hong, E. Y.-H. Charge-transfer processes in metal complexes enable luminescence and memory functions. *Nat. Rev. Chem.* **4**, 528-541 (2020).
24. Aliprandi, A., Mauro, M. & De Cola, L. Controlling and imaging biomimetic self-assembly. *Nature Chemistry* **8**, 10-15 (2015).
25. Herce, H. D. & Garcia, A. E. Molecular dynamics simulations suggest a mechanism for translocation of the HIV-1 TAT peptide across lipid membranes. *Proc. Natl. Acad. Sci. USA* **104**, 20805-20810 (2007).
26. Ng, D. Y. W. *et al.* Constructing Hybrid Protein Zymogens through Protective Dendritic Assembly. *Angew. Chem. Int. Ed.* **53**, 324-328 (2014).

27. Wong, V. C.-H. *et al.* Formation of 1D Infinite Chains Directed by Metal–Metal and/or π – π Stacking Interactions of Water-Soluble Platinum(II) 2,6-Bis(benzimidazol-2'-yl)pyridine Double Complex Salts. *J. Am. Chem. Soc.* **140**, 657-666 (2018).
28. Fleming, S. & Ulijn, R. V. Design of nanostructures based on aromatic peptide amphiphiles. *Chem. Soc. Rev.* **43**, 8150-8177 (2014).
29. Ranjbar, B. & Gill, P. Circular Dichroism Techniques: Biomolecular and Nanostructural Analyses- A Review. *Chem. Biol. Drug Des* **74**, 101-120 (2009).
30. Hu, H. *et al.* Phosphoinositide 3-Kinase Regulates Glycolysis through Mobilization of Aldolase from the Actin Cytoskeleton. *Cell* **164**, 433-446 (2016).
31. Park, J. S. *et al.* Mechanical regulation of glycolysis via cytoskeleton architecture. *Nature* **578**, 621-626 (2020).
32. Romero, P. *et al.* Computational prediction of human metabolic pathways from the complete human genome. *Genome Biol.* **6** (2004).
33. Divakaruni, A. S., Paradyse, A., Ferrick, D. A., Murphy, A. N. & Jastroch, M. Analysis and Interpretation of Microplate-Based Oxygen Consumption and pH Data. *Methods Enzymol.*, 309-354 (2014).
34. Trotta, A. P. *et al.* Disruption of mitochondrial electron transport chain function potentiates the pro-apoptotic effects of MAPK inhibition. *J. Biol. Chem.* **292**, 11727-11739 (2017).
35. Ippolito, L., Morandi, A., Giannoni, E. & Chiarugi, P. Lactate: A Metabolic Driver in the Tumour Landscape. *Trends Biochem. Sci.* **44**, 153-166 (2019).
36. Shiratori, R. *et al.* Glycolytic suppression dramatically changes the intracellular metabolic profile of multiple cancer cell lines in a mitochondrial metabolism-dependent manner. *Sci. Rep.* **9** (2019).
37. Hanahan, D. & Weinberg, Robert A. Hallmarks of Cancer: The Next Generation. *Cell* **144**, 646-674 (2011).
38. Rao, S. *et al.* AIF-regulated oxidative phosphorylation supports lung cancer development. *Cell Res.* **29**, 579-591 (2019).
39. Lanning, N. J. *et al.* Metabolic profiling of triple-negative breast cancer cells reveals metabolic vulnerabilities. *Cancer Metab.* **5** (2017).
40. Jia, D. *et al.* Elucidating cancer metabolic plasticity by coupling gene regulation with metabolic pathways. *Proc. Natl. Acad. Sci. USA* **116**, 3909-3918 (2019).
41. Vogelauer, M., Krall, A. S., McBrien, M. A., Li, J.-Y. & Kurdistani, S. K. Stimulation of Histone Deacetylase Activity by Metabolites of Intermediary Metabolism. *J. Biol. Chem.* **287**, 32006-32016 (2012).
42. Demchenko, A. P. Beyond annexin V: fluorescence response of cellular membranes to apoptosis. *Cytotechnology* **65**, 157-172 (2012).
43. Shen, D.-W., Pouliot, L. M., Hall, M. D., Gottesman, M. M. & Sibley, D. R. Cisplatin Resistance: A Cellular Self-Defense Mechanism Resulting from Multiple Epigenetic and Genetic Changes. *Pharmacol. Rev.* **64**, 706-721 (2012).

Methods

Synthesis and characterization of the complexes. Solid-phase peptide synthesis was conducted to prepare the alkynyl-functionalized peptidic precursors. Dehydrohalogenation reaction between the alkynyl group and a chloroplatinum (II) complex under an inert atmosphere led to the coordination of the alkynyl ligand to the Pt-tpy moiety to afford **1**, the precursor for **1-TAT** with a free boronic acid group. Linear conjugate **2** was synthesized, as a control, using a similar strategy. Complexation of **1** and the SHA-functionalized TAT peptide motif via SHA-boronic acid dynamic covalent bond was achieved by mixing them in a 1:1 molar ratio in a mixture of DMSO and phosphate buffer (PB, pH 7.4, 50 mM) (DMSO/PB, 2/98, vol%), leading to the formation of **1-TAT**. The compounds were identified by NMR spectroscopy, high-performance liquid chromatography, and mass spectrometry. A detailed procedure for the synthesis and characterization of the complexes can be found in the Supplementary Information.

LC-MS analysis of H₂O₂-induced conversion. Complex **1** was dissolved in a mixture of NH₄HCO₃ buffer (pH 7.4, 20 mM) and CH₃OH (90/10, vol%) at a concentration of 100 μ M. Equal volume of H₂O₂ (1 mM) solution in a mixture of NH₄HCO₃ buffer (pH 7.4, 20 mM) and CH₃OH (90/10, vol%) was added to initiate the conversion. LC-MS analysis of the mixture was performed on a Shimadzu LC-MS 2020 equipped with a Kinetex EVO C18 column (50 \times 2.1 mm, 2.6 μ m, 100 Å), an SPD-20A UV-Vis detector, and an electrospray ionization source. MilliQ water, acidified with 0.1% formic acid, and CH₃CN were used as solvents for all measurements. The solvent gradient started with 5% CH₃CN and 95% water. This solvent ratio was kept constant for 2 min, and then the CH₃CN content was linearly increased to 95% over 14 min. The molar ratio of the compounds was calculated using peak areas at 254 nm.

Self-assembly formation of 2_{NF}. Monomeric complex **2** was dissolved in DMSO at a high concentration (10 mM) before diluted to different concentrations using PB (pH 7.4, 50 mM). Self-assembly was induced by agitating the solution in an Eppendorf Thermomixer for 2 h at 37 °C at 500 r.p.m.

TEM analysis. TEM samples were prepared by dropping a solution of **2_{NF}** onto a carbon-coated copper grid. After 5 min, the excess solution was removed by a filter paper. The sample was then stained inverting the TEM grid (sample side down) on a droplet (10 μ L) of 2% uranyl acetate solution for 30 seconds. After removing the staining solution with a filter paper, the sample was washed with Milli-Q water for three times (shaken in water for 6 seconds for each time). After drying in air, the measurement was conducted on a JEOL JEM-1400 TEM operating at an accelerating voltage of 120 kV.

SAED Analysis. Sample for SAED analysis was prepared by drop-casting a solution of **2_{NF}** in H₂O on an ultrathin carbon grid. SAED analysis was performed on an image-side aberration-corrected FEI Titan 80-300 operated at 300 kV. The microscope is equipped with a CEOS hexapole aberration-corrector which corrects the geometrical axial aberrations up to the 3rd-order. Diffraction data acquisition was conducted on a Gatan UltraScan CCD camera. For SAED acquisition, we used a selected-area aperture with a physical diameter of 50 μ m, corresponding to a diameter of 700 nm in the image plane. In order to avoid substantial electron radiation damage on the specimen, a low-dose technique has been applied. The total electron dose for SAED acquisition was 0.8 e-/Å² (dose rate: 0.04 e-/Å²s, acquisition time: 20 s).

Cryo-TEM analysis. For cryo-TEM examinations the sample was prepared using a Mark V Vitrobot® (Thermo Fisher Scientific) cryo plunge device. Samples were plunged from a climate chamber operated at room temperature with 100 % relative humidity. The sample dispersion was applied either to a Quantifoil® or lacey holey carbon grid and plunged into liquid ethane. Subsequently, the specimen grid was transferred to a Titan Krios G4 TEM (Thermo Fisher Scientific). Images were acquired using a Gatan K3 direct detection camera.

¹H, ¹H NOESY NMR experiments. The NOESY NMR measurements were performed with a 5 mm QXI ¹H/¹³C/¹⁵N/³¹P probe equipped with a z-gradient on the 850 MHz Bruker AVANCE III system. The spectroscopic

widths of the ^1H , ^1H NOESY experiments were 13500 Hz (850 MHz; 16 ppm) in both dimension (f1 and f2) and the relaxation delay is 2 s. The mixing time was kept at 300ms. A detailed analysis for the NOESY NMR experiments can be found in the Supplementary Information.

Cell culture. A549 and MDA-MB-231 cells were cultured at 37 °C and 5% CO_2 in Dulbecco's Modified Eagle's Medium (DMEM, high glucose), supplemented with 10% FBS. Both cell lines were cultured in T75 culture flask and subcultivated two to three times per week.

Cellular uptake studies. A549 and MDA-MB-231 cells were seeded at a density of 25,000 cells/well in an 8-well confocal plate. After adhering for 24 h, cells were treated with the sample for 4 h at 37 °C. Before adding to the cells, samples were pre-incubated to form the **1-TAT** by dissolving **1** in DMSO and mixing with an equimolar amount of the TAT peptide, which was dissolved in Dulbecco's PBS. The sample was further diluted with DPBS to a final volume of 40 μL (DMSO/DPBS, 10/90, vol%). Sample solutions were further diluted 1:4 with DMEM and added to the cells (total DMSO content = 2%), after removing the existing medium from the wells. After the incubation time was over, the cell nucleus was stained with Hoechst 33342 dye for 20 min at 37 °C. A459 cells were additionally treated with Phalloidin-iFluor™ 405 instead of the Hoechst 33342 dye to stain the cytoskeleton. The staining solution was removed, and fresh FluoroBrite DMEM Medium was added to the cells before they were imaged by confocal laser scanning microscopy. Confocal images of cells were taken on a Leica TCS SP5 and Visitron Spinning Disc microscope. To monitor the Hoechst, DAPI and Phalloidin dyes, a 405 nm excitation diode laser was used with an emission filter from 415-500 nm. For Annexin-FITC, an Argon laser was used for excitation at 488 nm with an emission filter from 500-600 nm. To study the uptake of the compound **1-TAT** and subsequent formation of **2_{NF}**, a DPSS laser was used at 561 nm excitation and an emission range from 600-800 nm.

CLEM studies. One day before treatment, cells were seeded and grown on carbon pre-coated sapphire disks (3 mm; M. Wohlwend GmbH), which were sterilized and oxygen plasma cleaned before use (30 s, 0.2 mbar, 20% power; Femto, diener electronic). The disks were placed in a 24-well plate with 50,000 cells/well, which was incubated at 37°C, 5% CO_2 overnight. After incubation with **1-TAT** (50 μM , 6h), each sapphire disk was collected and slightly immersed into 1-hexadecene before placing them between two aluminum plates (3 mm, Plano). The aluminum plates with the sample were placed into a specimen holder for high pressure freezing in a Wohlwend HPF Compact 01 high-pressure freezer with a pressure of 2100 bar for 2–3 s. The specimen holder was withdrawn from the freezer and immersed into liquid nitrogen to release the sample. The frozen sample was then stored in a container filled with liquid nitrogen. Subsequently, freeze substitution of the sample was carried out in a 0.5 mL Eppendorf tube using an AFS2 freeze substitution unit (Leica). Each tube contained freeze substitution solution, consisting of 0.2wt/vol% osmium tetroxide, 0.1wt/vol% uranyl acetate, and 5% distilled water in acetone. The tubes were firstly kept at –90 °C and automatically warmed up to 0 °C in 24 h. After keeping at room temperature for 1 h, the substitution solution was removed, and the samples were washed three times with acetone. Each sample was infiltrated in an ascending epoxy resin series (30%, 50%, and 75% in acetone) for 1 h before final infiltration in 100% epoxy resin overnight. Subsequently, each sample was transferred into a new Eppendorf tube containing freshly prepared pure epoxy resin for polymerization at 60 °C for 72 h. After polymerization, sample blocks were kept at room temperature until their sectioning. Sample blocks for each time point were trimmed and sectioned into 100 nm sections by a 35° diamond knife (Diatome) in EM UC6 ultramicrotome (Leica). Sections were then carefully placed onto H6 copper finder grids (Plano) and imaged on a confocal light microscope (Leica SP5) using 561 nm excitation and a 610/60 ET bandpass. For later registration to TEM images, transmitted light and reflected light images were simultaneously recorded. Electron microscopy images were collected on a Jeol 1400 120kV using a 2K bottom mount CCD camera and a Tecnai F20 200 kV TEM by FEI using a K2 Gatan camera. The TEM images were stitched to show the entire cell. Registration of light and electron microscopy images was done by manual landmark registration on entire cells using ImageJ. Landmark selection was based on features identified in the reflected light and transmitted light images.

Cell metabolism assay. The effect of the compounds on the cell metabolism of A549 and MDA-MB-231 was investigated using the Agilent Seahorse XFe96 Analyzer. Cells were seeded first in DMEM one day before the assay and incubated overnight at 37°C, 5% CO₂. The cartridge for sample loading was loaded with calibration solution (200 µL per well) and incubated at 37°C in a non-CO₂ incubator. On the day of the assay, XF DMEM, pH 7.4 was supplemented with supplements according to the specific assay kit. Cells were washed once with XF DMEM (200 µL) and the medium was substituted with fresh XF DMEM (180 µL) and placed in a 37°C non-CO₂ incubator for 45 to 60 minutes. The cartridge was prepared by loading the samples (20 µL) in Port A of each well and the components of the performed assay in Ports B-D. The cartridge and 96-well plate with the cells were loaded in the instrument and the content of the ports was injected sequentially according to the specific assay. The pH, to monitor the extracellular acidification rate (ECAR) and the oxygen concentration, or to monitor the oxygen consumption rate (OCR) were constantly measured throughout the entire time of the assay.

For the Mito stress assay, ports B-D were loaded with Oligomycin (22 µL), Carbonyl cyanide-4 (trifluoromethoxy) phenylhydrazone (FCCP) (25 µL), and a mixture of Rotenone and Antimycin A (Rot/AA) (27 µL). After loading the cell plate eight measurement cycles were performed as baseline control. After addition of the compound, twenty-five measurement cycles were performed before the components of the Mito stress assay were added. For each component five measurement cycles were performed.

For the glycolysis stress assay, cells were maintained for 1 h in Seahorse DMEM supplemented only with glutamine before the assay. Ports B-D were loaded with glucose (22 µL), Oligomycin (25 µL), and 2-Deoxyglucose (27 µL). After loading the cell plate eight measurement cycles were performed as baseline control. After addition of the compound twenty-five measurement cycles were performed before the components of the glycolysis stress assay were added. For each component five measurement cycles were performed.

Cell viability assay. A549 and MDA-MB-231 cells were both seeded at a density of 2,500 cells/well in a white half area 96-well plate and incubated at 37°C overnight to allow them to adhere. On the next day, different concentrations of the **1-TAT** or cisplatin were prepared in PBS at a 10x concentration of the final concentration, and this solution (20 µL) was added to a fresh medium (180 µL). The old medium of the cells was removed and substituted with a fresh medium (50 µL) containing different concentrations of sample, prepared as described before. For each condition, triplicates were performed. Cells were incubated with the sample for 4 h or 24 h. After the treatment, CellTiter-Glo® Assay solution (50 µL) was added to each well, and the plate was placed on an orbital shaker for 2 minutes and subsequently incubated 10 minutes at room temperature. Luminescence was measured using a Promega GloMax®-Multi Detection System using manufacturer's protocol.

Acknowledgements

The authors gratefully acknowledge financial support from the Max Planck-Bristol Centre for Minimal Biology. Z. Z. is supported by the Alexander von Humboldt Foundation. P.M. acknowledge the support from SFB 1066 B16 (Grant No 213555243). D.M., H.Q. and U.K. gratefully acknowledge the funding from the Germany Research Foundation (DFG) in SFB-1415 (Grant No. 417590517) and from the European Union's Horizon2020 research and innovation programme under Grant Agreement No. 881603 (GrapheneCore3).

Author contributions

Z.Z., D.Y.W.N and T.W. conceived and designed experiments. Z.Z. synthesized the compounds, conducted the kinetic and self-assembly analysis. K.M. and D.Y.W.N. performed the cellular studies. K.M. and P.M. conducted the cellular metabolism assay. S.X., Y.W., and C.J.W. assisted with microscopy analysis. L.X. assisted with

chemical synthesis. A.K., S.H., and K.L. conducted the CLEM analysis. D.N., H.Q., and U.K. performed the selected-area electron diffraction analysis. M.W. provided the NMR expertise. I.L. and K.L. conducted the cryo-TEM analysis. Z.Z., K.M., and D.Y.W.N. wrote the manuscript. D.Y.W.N. and T.W. supervised the project and corrected the manuscript. All authors read and approved the final manuscript.